PAPER • OPEN ACCESS

SOLPS-ITER analysis of a proposed STEP double null geometry: impact of the degree of disconnection on power-sharing

To cite this article: R.T. Osawa *et al* 2023 *Nucl. Fusion* **63** 076032

View the article online for updates and enhancements.

SOLPS-ITER analysis of a proposed STEP double null geometry: impact of the degree of disconnection on power-sharing

R.T. Osawa[1,*], D. Moulton[1], S.L. Newton[1], S.S. Henderson[1] ⬤, B. Lipschultz[2] ⬤ and A. Hudoba[1]

[1] UKAEA-CCFE, Culham Science Centre, Abingdon OX14 3DB, United Kingdom of Great Britain and Northern Ireland
[2] Department of Physics, University of York, Heslington, York YO10 5DD, United Kingdom of Great Britain and Northern Ireland

E-mail: ryoko.osawa@ukaea.uk

CrossMark

Abstract

To mitigate the issue of plasma exhaust in reactor scale tight aspect ratio tokamaks such as Spherical Tokamak for Energy Production (STEP), a double-null (DN) configuration is thought to be advantageous over a single-null (SN) configuration. However, practical control of the plasma vertical stability will likely lead to an oscillation around the symmetry point, which may lead to transient loading of the divertors. In this work we investigated the impact of disconnection of the two separatrices δR_{sep} on the power-sharing between the divertors in disconnected-double-null configurations for the initial iteration of STEP design using the SOLPS-ITER code without drifts. The power fraction to the primary divertor increased with δR_{sep}, reaching ∼95% at the highest δR_{sep} which is representative of SN. The total power fraction to the inner divertors (upper + lower), however, did not show an increase with δR_{sep} for $\delta R_{\text{sep}}/\lambda_q \leqslant 2$, where λ_q is the parallel heat flux decay length, and even at the highest δR_{sep} it showed only ∼30% increase from connected-double-null (CDN), unlike the experimental results for current conventional aspect ratio machines. We found two underlying mechanisms that could explain this result—the total flux compression from the outer midplane to the primary inner divertor target and the parallel current in the primary SOL (between the two separatrices). This work implies that the benefit of DN over SN in power load onto the inner divertor in STEP may be less than found experimentally in conventional tokamaks due to its tight aspect ratio. Further investigations through experiments, especially on STs and simulations with additional physics such as drifts, are the subject of a future investigation.

---

* Author to whom any correspondence should be addressed.

1. Introduction

Plasma exhaust is a key challenge for the Spherical Tokamak for Energy Production (STEP) programme [1]. As STEP aims at producing net energy from a prototype fusion energy plant, the power crossing the separatrix in STEP can be much larger than that handled in existing experimental devices. In a single-null (SN) configuration, combined with the low aspect ratio of a spherical tokamak (ST) ($R/a \sim 1.6$), the situation is difficult for the inner divertor target due to the small radius of the strike point and limited space for power mitigation.

To avoid this, we have been assessing a double-null (DN) configuration as a promising solution for STEP, as the majority of the power can flow into the outer targets which can be located at large major radius. This benefit of DN can be especially beneficial for STs where the situation for the inner divertor targets is difficult as described above. However, practical control of the plasma vertical stability will likely lead to an oscillation around the perfect symmetry point, where both X-points exist on the last closed flux surface. This leads to a disconnected double-null (DDN) configuration that has a gap between the two separatrices.

This gap, usually quantified by the distance between the two separatrices at the outer-midplane (OMP) δR_{sep}, could be a critical matter for the primary inner target in DDN. In a connected double-null configuration (CDN), power from the OMP flows towards the two outer divertors. In DDN, on the other hand, the inner and outer targets are now linked by magnetic field lines, i.e. the power from the OMP can partly flow to the primary inner divertor. Furthermore, if δR_{sep} reaches values similar to the radial exponential decay length of the SOL at the midplane, it would lead to near SN loads onto the primary inner divertor target. The increase of the inflow power can be critical for the inner target in a ST due to the small radius of the strike point and limited space.

To assess the impact of disconnection, several experimental studies and a few numerical/theoretical studies have been carried out so far. As a numerical study, the B2.5 code [2] was used in DDN geometries of the Tokamak de Varennes, which showed pronounced up-down asymmetry on the outer targets even with a relatively small level of disconnection [3]. As for the experimental studies, the power asymmetry was assessed on MAST in L-mode discharges [4], and also in H-mode discharges [5, 6]. In CDN ($\delta R_{\mathrm{sep}} \sim 0$), the power fraction to the inner was $\sim$5% in the L-mode and during edge-localised modes (ELMs) in H-mode. During the inter-ELM periods at low ELM frequency in H-mode, the fraction became roughly the ratio of separatrix surface area ($\sim$20%). In L-mode, dependence of in-out power-sharing on δR_{sep} was observed and the ratio was different between lower and upper

SN discharges [4]—the fraction to the inner was $\sim$20% for the lower SN, whilst $\sim$10% for the upper SN, which implied a contribution of $\nabla \mathbf{B}$ drift which directed downwards for ions in this case. Another important fact here is that the fraction to the inner $\sim$20% is lower than that reported in similar experiments on conventional aspect ratio tokamaks such as DIII-D [7, 8] (H-mode) and Alcator C-Mod (L-mode) [9] where $\sim$30% of the power flows to the inner divertors in SN discharges. The influence of the confinement regime was also reported on Alcator C-Mod [9]: As it changed from SN to CDN, the fraction to the inner changed $\sim$30%–$\sim$5% in L-mode, whilst it changed $\sim$40%–$\sim$20% in H-mode.

In addition, to assess the dependence of the power-sharing on δR_{sep} in a more quantitative way, semi-analytic formulations to describe the dependence of the power-sharing were introduced in [9]—we call this set of formulations 'Brunner's model' hereafter in this paper. In addition, they suggested a scaling function of parameters in the model for other machines which has dependence on parallel heat flux decay length λ_q and poloidal magnetic field B_p. Using that scaling, the Brunner's model was applied to STEP that has similar λ_q and larger B_p compared to Alcator C-Mod. This work suggested that null balance to better than 1 mm is required for STEP.

The ultimate goal is to clarify the benefits of DN in terms of plasma exhaust compared to SN and understand the underlying mechanisms that dictate the power balance in DDN. Towards this goal, the research presented here includes our analysis of the impact of δR_{sep} ($\geqslant$0) on the power-sharing in STEP.

This paper is organised as follows. Section 2 introduces the SOLPS-ITER (the ITER-hosted version of the scrape-off layer plasma simulator SOLPS) simulation setup for a δR_{sep} scan we performed in this study. Then in section 3, a description of a part of Brunner's model is given, which is used in this study to better understand the numerical results of the up-down power-sharing. The simulation results are given in section 4, for the up-down power-sharing (section 4.1) and for the in-out power-sharing (section 4.2). As for the up-down sharing, the power fraction to the primary divertor (upper divertor in the investigated cases) increased with δR_{sep}, reaching $\sim$95% at the highest δR_{sep} which is representative of SN. As for the in-out power-sharing, however, the total power fraction to the inner divertors (upper + lower), did not show an increase with δR_{sep} for $\delta R_{\mathrm{sep}}/\lambda_q \leqslant 2$, where λ_q is the parallel heat flux decay length at the outer mid-plane, and even at the highest δR_{sep} it showed only $\sim$30% increase from CDN, unlike the experimental results for current machines. To further analyse the in-out power-sharing, section 4.2 is divided into three subsections, section 4.2.1 for the radial heat transport through the primary separatrix, section 4.2.2 for the power loss in the

main SOL, and section 4.2.3 for the parallel heat transport in the primary SOL. Two important effects that reduced the power fraction to the inner divertor in the primary SOL are further discussed separately—the total flux expansion/compression (section 4.2.3.1) and the parallel current (section 4.2.3.2). Further discussions for the parallel current and the ballooning effect are given in section 5 and conclusions are given in section 6.

2. SOLPS-ITER setup

SOLPS-ITER [10–12] is an integrated code, incorporating the multi-species fluid code B2.5 and the kinetic Monte-Carlo neutral code EIRENE. We utilised this code to model the initial design of STEP with upper-primary DDN configurations. The equilibrium of this design has the following parameters: R (major radius) = 2.55 m, r (minor radius) = 1.55 m, A (aspect ratio, R/a) = 1.64, I_p (toroidal plasma current) = 16.5 MA, B_0 (Toroidal field) = 1.79 T, and κ (elongation) = 2.89. Since drifts are not switched on, the analysis is identical when using the upper or lower divertor as the primary divertor. The distance between the two separatrices, δR_{sep}, was scanned stepwise from 0 mm to 4 mm, with the parallel heat flux decay length $\lambda_q \sim 2$ mm across the scan.

The numerical grid for the $\delta R_{sep} = 2$ mm case is shown in figure 1. For around 1.0 GW fusion power with Q = fusion power/auxiliary power $\approx$10% and 70% core radiation, one can figure out the power crossing the separatrix is $\sim$100 MW. The energy flux at the core boundary was therefore set as $P_{in} = 100$ MW, divided equally between ions and electrons. By dividing the fusion power (1.0 GW) by the energy released per reaction (2.8×10^{12} J = 17.6 MeV), we obtain an expected helium production rate $\alpha = 3.5 \times 10^{20}$ s^{-1}. Given this number, the ion particle flux through the core boundary Γ_{in} was set $\Gamma_{in} = 3.5 \times 10^{22}$ s^{-1}, based on the simulations on ITER which set this flux consistent with core fuelling and fusion power production [13]. The radial particle transport coefficient $D_\perp$ and the radial heat transport coefficient for the ions and the electrons $\chi_\perp$ were set to be $D_\perp = 0.3$ m^2 s^{-1} and $\chi_\perp = 1.0$ m^2 s^{-1}, respectively. The flux limiters were activated for the electron parallel heat flux (0.3) and for the parallel ion viscous limiter (0.5).

The wall geometry and all puff/pump locations were set to be up-down symmetric (figure 1). Thus, the inputs to the CDN case ($\delta R_{sep} = 0$ mm) were perfectly up-down symmetric including the equilibrium. Puffing slots of deuterium molecules (D2) were placed in the top/bottom Private Flux region (PFR) near the X-points. To get the target loads down to manageable level, argon (Ar) gas was seeded from the PFR-side corner of the outer targets, as shown in figure 1. In B2.5, all the charge states of argon were individually solved as well as the deuterium ion. The pumping ducts were set in the outer legs (two ducts in total) and the pumping speed was set as 131 m^3 s^{-1} for each duct, independently of pumped species. The tungsten wall temperature of the duct and the pumping
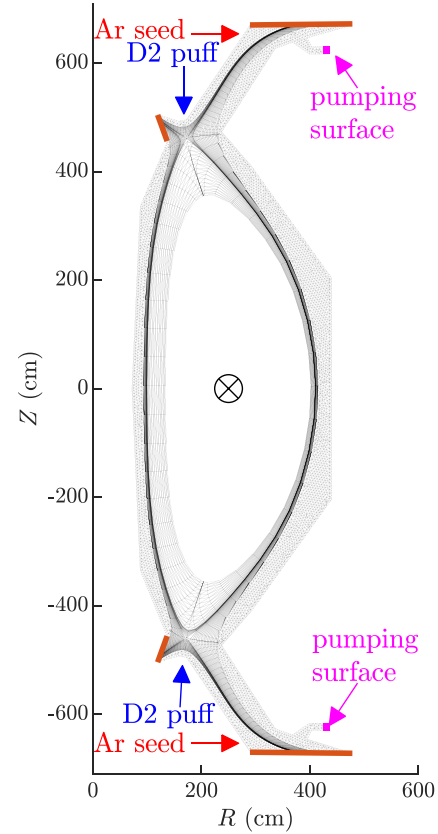
Figure 1. The grid, puffing/seeding and pumping locations in SOLPS-ITER for $\delta R_{sep} = 2$ mm cases.

tube was set to 306.85 °C (0.049 98 eV), while it was set to 857.85 °C (0.097 49 eV) for the rest of the wall, expecting it to run warm. The sputtering of the wall was not modelled in the simulations.

All drift terms were deactivated in this study. Some studies on assessing effects due to the drifts are ongoing, which are briefly summarised in section 5.3 and will be reported elsewhere in the future. While the drifts were deactivated, the currents (parallel currents and a small anomalous radial current) were activated in the plasma solver.

3. Brunner's model

Brunner's model [9] was formulated to estimate power-sharing between the four divertors in DDN (figure 2(*a*)). It consists of two parts, (1) in-out sharing and (2) up-down sharing. For the power-sharing we consider the power flowing into each divertor, rather than that reaching each divertor target after dissipation. Thus we define the power flowing into each divertor entrance (the surfaces $A, B, C,$ and D in figure 2(*a*)) as P_{uide}, P_{uode}, P_{lide}, and P_{lode}, for the upper-inner, upper-outer, lower-inner, and the lower-outer divertor entrances, respectively. The power coming through the separatrix P_{sep} is split between the four divertors and the side walls. Assuming that the fraction to
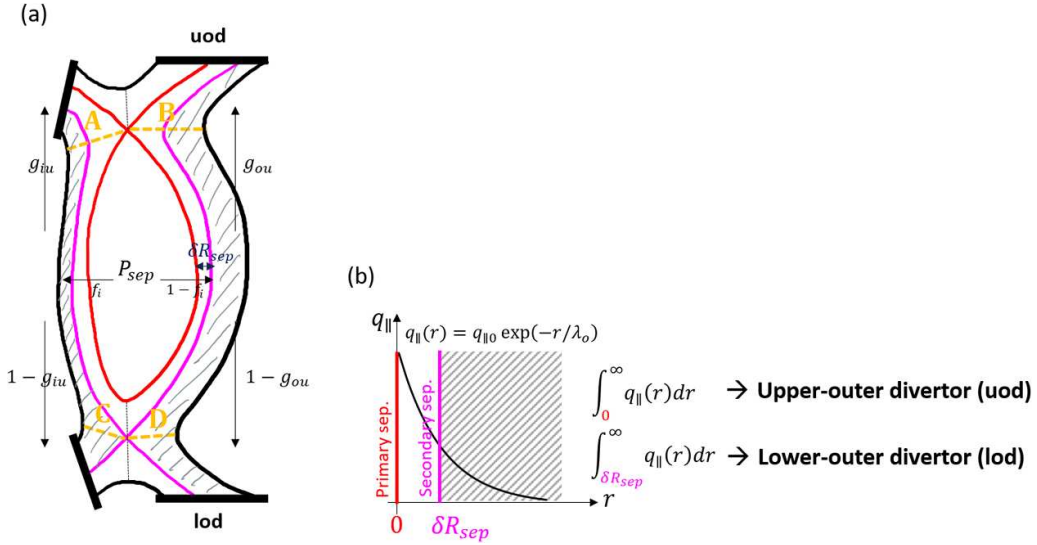
Figure 2. (*a*) Schematic view of Brunner's model—a model for power-sharing between four divertors in DDN. (*b*) Assumed profile of the parallel heat flux along the outer midplane in the model.

the side walls is negligibly small and there is no radiation in the SOL in the steady state we have:

$$P_{\text{sep}} \sim P_{\text{dive,tot}} = P_{\text{lide}} + P_{\text{uide}} + P_{\text{uode}} + P_{\text{lode}}. \quad (1)$$

In-out sharing is defined with f_{i}, the power fraction going to the inner divertors, as

$$f_{\text{i}} = \frac{(P_{\text{lide}} + P_{\text{uide}})}{P_{\text{dive,tot}}}. \quad (2)$$

The in-out sharing is followed by up-down sharing separately for the outer and inner divertors. For the outer divertors, it is defined by g_{ou}, the power fraction going to the upper-outer divertor (UOD), such that

$$g_{\text{ou}} = \frac{P_{\text{uode}}}{(P_{\text{uode}} + P_{\text{lode}})}. \quad (3)$$

A theoretical expression for g_{ou} can be obtained by the assumptions that (1) the parallel heat flux density decays exponentially with a characteristic length λ_{o} at the outer midplane and (2) the power crossing the secondary separatrix is equally divided amongst the upper and the lower divertors. From the first assumption, we can describe the power going to the UOD (from the OMP) as

$$P_{\text{uode}} = \int_0^\infty q_{||}(r)\mathrm{d}r. \quad (4)$$

From the second assumption, the power going to the lower-outer divertor is equal to that going to the upper-outer via the secondary SOL, thus

$$P_{\text{lode}} = \int_{\delta R_{\text{sep}}}^\infty q_{||}(r)\mathrm{d}r. \quad (5)$$

This gives us the theoretical expression of g_{ou},

$$g_{\text{ou}} = \frac{\int_0^\infty q_{||}(r)\mathrm{d}r}{\int_0^\infty q_{||}(r)\mathrm{d}r + \int_{\delta R_{\text{sep}}}^\infty q_{||}(r)\mathrm{d}r} = \frac{\exp(\delta R_{\text{sep}}/\lambda_{\text{o}})}{1 + \exp(\delta R_{\text{sep}}/\lambda_{\text{o}})}. \quad (6)$$

As for the inboard side, one may think that the same model for the outboard side cannot be applied, because a large part of the power to the inner divertors could originate as power from the LFS in addition to the radial power from the HFS. Despite this, equation (6) was found reasonable also to describe the up-down power-sharing of the inner divertors in the experimental results of [9], as long as a different decay length parameter, λ_{i} instead of λ_{o}, is taken into account. The power fraction to the upper-inner divertor (UID) g_{iu} then is described as

$$g_{\text{iu}} = \frac{\exp(\delta R_{\text{sep}}/\lambda_{\text{i}})}{1 + \exp(\delta R_{\text{sep}}/\lambda_{\text{i}})} = \frac{\exp(\delta R_{\text{sep,inn}}/\lambda_{\text{i,inn}})}{1 + \exp(\delta R_{\text{sep,inn}}/\lambda_{\text{i,inn}})}. \quad (7)$$

Here we introduced $\delta R_{\text{sep,inn}}$, the distance between the two separatrices at the inner midplane (IMP), and $\lambda_{\text{i,inn}}$, the corresponding parameter for the inboard up-down power-sharing. They can be described as

$$\delta R_{\text{sep,inn}} = \alpha_{\text{pol}}\delta R_{\text{sep}}, \quad \lambda_{\text{i,inn}} = \alpha_{\text{pol}}\lambda_{\text{i}}, \quad (8)$$

where α_{pol} is a poloidal flux expansion from the OMP to the IMP.

To summarise, the power going to each divertor is given by the model to be:

- Lower-inner: $f_{\text{i}}(1 - g_{\text{iu}})$
- Upper-inner: $f_{\text{i}}g_{\text{iu}}$
- Upper-outer: $(1 - f_{\text{i}})g_{\text{ou}}$
- Lower-outer: $(1 - f_{\text{i}})(1 - g_{\text{ou}})$

Table 1. Correspondence between Brunner's model and SOLPS-ITER.

	Description in the model	SOLPS-ITER
g_{ou}	$\dfrac{\exp\left(\delta R_{sep}/\lambda_o\right)}{1+\exp\left(\delta R_{sep}/\lambda_o\right)}$	$\dfrac{P_{uode}}{\left(P_{uode}+P_{lode}\right)}$
g_{iu}	$\dfrac{\exp\left(\delta R_{sep}/\lambda_i\right)}{1+\exp\left(\delta R_{sep}/\lambda_i\right)} = \dfrac{\exp\left(\delta R_{sep,inn}/\lambda_{i,inn}\right)}{1+\exp\left(\delta R_{sep,inn}/\lambda_{i,inn}\right)}$	$\dfrac{P_{uide}}{\left(P_{uide}+P_{lide}\right)}$

In this study, we use the second part of Brunner's model, the model for the up-down power-sharing with g_{ou} and g_{iu}. The correspondence between the model definitions and the SOLPS-ITER quantities is shown in table 1.

4. SOLPS-ITER modelling results

The cases performed in this study are detailed in table 2. In the steady state, the target electron temperature at the strike point ranges from 1 eV to 2 eV for the inner divertors, from 0.5 to ∼20 eV for the outer divertors, which supports that most of the cases are not far from the operational regime. However, the peak temperature at the primary inner target remained high (∼30 eV) in the far SOL in all the cases, because of the feature of vertical targets. The inputs were up-down symmetric, except for the equilibria for the DDN cases ($\delta R_{sep} > 0$ mm).

Figures 3(*a*) and (*b*) show the SOLPS-ITER predictions of power-sharing between the four divertors as a function of δR_{sep}. To support the color map shown in figure 3(*a*), the ratio to each divertor is shown in figure 3(*b*). The features of the power-sharing were consistent across the cases, thus the result of Case No. 3 is shown here as a representative in both figures.

To better understand these figures, we will first focus on up-down power-sharing, investigating how well the SOLPS-ITER results follow Brunner's model. Brunner's model has a single unknown parameter for the up-down sharing for each side, λ_o for the outboard and λ_i ($\lambda_{i,inn}$) for the inboard side, as shown in equations (6) and (7). We quantify the agreement with Brunner's model by fitting the parameters λ_o and $\lambda_{i,inn}$ to the simulation data of up-down sharing, and comparing those fitted values to the actual parallel heat flux decay lengths in the simulation, $\lambda_{q,out}$ for the outboard and $\lambda_{q,inn}$ for the inboard.

Secondly we study in-out power-sharing. An interesting finding in figure 3(*a*) is that the total power fraction to the inner divertors, f_i in equation (2) shown by the boundary between the green and the blue colors, does not increase for $\delta R_{sep} \leqslant 4$ mm, corresponding to $\delta R_{sep}/\lambda_{q,out} \leqslant 2$, though the power ratio to the UID slightly increases as shown in figure 3(*b*), which is unlike the experimental results [4, 9]. To understand the physical mechanisms producing this behaviour, two different sources/sinks that are not in the model have been examined: the radial heat flux through the primary separatrix (section 4.2) and the parallel energy transport in the primary SOL which links inboard and outboard sides (section 4.2.3). Only the results of $0 \leqslant \delta R_{sep}/\lambda_{q,out} \leqslant 2$ ($0 \leqslant \delta R_{sep} \leqslant 4$ mm) will be assessed in detail for the in-out sharing.

One may think that the use of the constant radial transport coefficients could be a major cause of the discrepancies between the simulation results and the experimental results. The impact of the ballooning effect, i.e. the use of spatially-varying transport coefficients with a function of the magnetic field $\propto 1/B^k$, will be discussed in section 5.2. In addition, brief summaries of recent works looking at effects due to drifts will be given in section 5.3.

4.1. UP-DOWN sharing

Power-sharing between the upper and lower divertor was investigated separately for the outboard and the inboard side. The total energy flux at each divertor entrance, which was used for calculating the power-sharing, is well-represented by the summation of the total conduction Q_{cond}, total convection Q_{conv}, and the energy flux carried by the electron thermal current Q_{thermj}, such that

$$Q_{tot} = Q_{cond} + Q_{conv} + Q_{thermj}, \qquad (9)$$

where

$$Q_{cond} = Q_{conde} + Q_{condi} = -A_{\parallel}\left(\kappa_{\parallel e}b_x^2\frac{\partial T_e}{h_x\partial x} + \kappa_{\parallel i}b_x^2\frac{\partial T_i}{h_x\partial x}\right), \qquad (10)$$

$$Q_{conv} = Q_{conve} + Q_{convi}$$
$$= A_{\parallel}b_x\left(\frac{5}{2}nT_e(V_{\parallel}-j_{\parallel}/en) + \Sigma_a\frac{5}{2}n_aT_iV_{a\parallel}\right), \quad (11)$$

$$Q_{thermj} = -A_{\parallel}b_x\left(0.71j_{\parallel}T_e/e\right). \qquad (12)$$
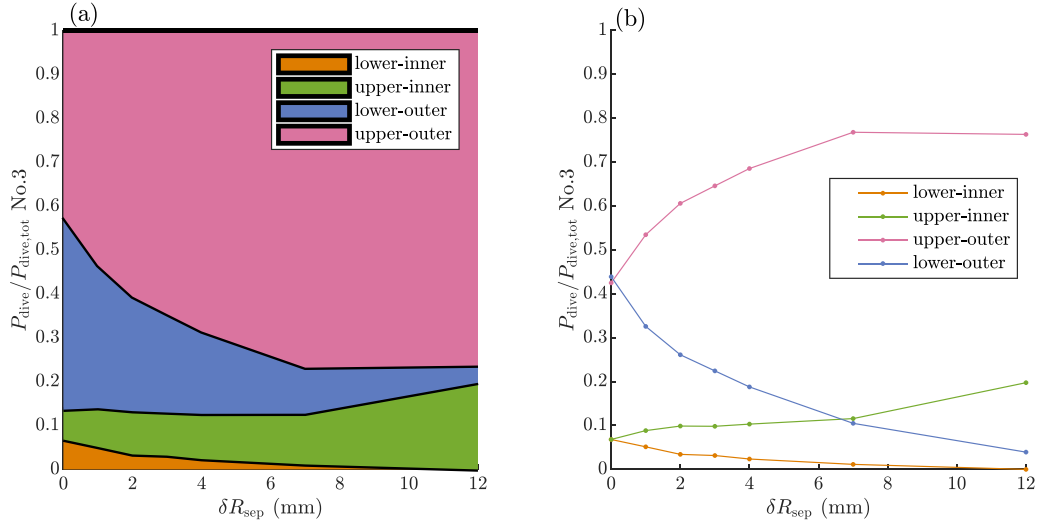
Here $A_{\parallel}$ is the parallel area, $\kappa_{\parallel e}$ and $\kappa_{\parallel i}$ are the parallel conductivity for the electron and D ion respectively, $b_x = B_x/B$ with B_x the poloidal magnetic field, x is the poloidal coordinate, h_x is the metric coefficient for the poloidal coordinate, and $T_e, T_i, n, V_{\parallel}, n_a, V_{a\parallel}, j_{\parallel}$, and e are the electron and ion temperature, electron density, D$^+$ parallel flow velocity, density for ion species a, parallel velocity for ion species a, the parallel current, and the unit of charge, respectively.

Figure 4(*a*) shows the power fraction to the upper divertor for the outboard side, g_{ou}. The dependence of g_{ou} on δR_{sep} follows the model for the choice of λ_o in the model within the range 2 mm $\leqslant \lambda_o \leqslant$ 4 mm. As for the inboard side in figure 4(*b*), the power fraction to the upper divertor g_{iu} is plotted as a function of the distance of the two separatrices on the inboard side, $\delta R_{sep,inn}$. The simulation results are well-fitted by using $\lambda_{i,inn} \sim 10$ mm.

Now we want to know if those parameters λ_o and $\lambda_{i,inn}$ are similar to the parallel heat flux decay lengths in the simulation. The parallel heat flux decay lengths $\lambda_{q,out}$ and $\lambda_{q,inn}$ were calculated in the following steps for the outboard side and the inboard side, respectively : (i) obtain the total energy flux at the primary divertor entrance, (ii) divide the total energy flux by the parallel area at the midplane, (iii) map the total energy flux density to the midplane. As shown in figure 5, the parallel heat flux decay length on the outboard side appears to be a relatively

Table 2. Investigated cases in SOLPS-ITER. The four different colors will be used in some figures hereafter such as figure 4 to distinguish the cases (Case No. 1–4).

Case No.	D2 puff ($\times 10^{23}$ s^{-1})	Ar puff ($\times 10^{21}$ s^{-1})	δR_{sep} (mm)						
			0	1	2	3	4	7	12
1	2.0	6	—	✓	✓	✓	✓	—	—
2	2.0	8	—	✓	✓	✓	✓	✓	✓
3	3.0	8	✓	✓	✓	✓	✓	✓	✓
4	3.0	10	✓	✓	✓	✓	✓	—	—

Figure 3. SOLPS-ITER predictions of power-sharing between the four divertors $P_{\text{dive}}/P_{\text{dive,tot}}$ as a function of δR_{sep} for Case No. 3 in table 2, shown by (*a*) area map and by (*b*) individual plots of the ratio.
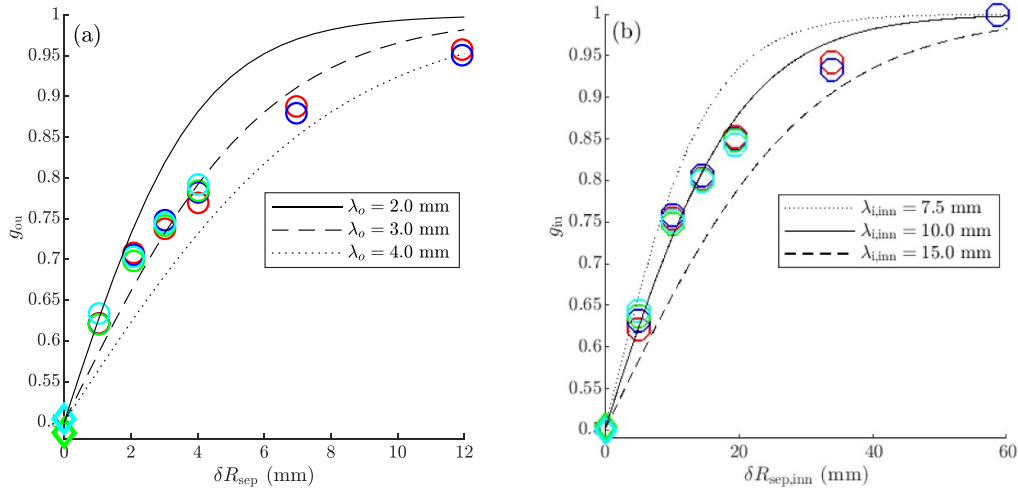
Figure 4. Power fraction to the upper divertor for (*a*) the outboard side, g_{ou} and (*b*) the inboard side, g_{iu}. Markers are SOLPS-ITER simulation results whose colors correspond to those in table 2.

good estimation ($\lambda_{\text{q,out}} \approx \lambda_{\text{o}}$) while that on the inboard side shows a significant mismatch between them ($\lambda_{\text{q,inn}} \ll \lambda_{\text{i}}$).

The observed relationships, $\lambda_{\text{q,out}} \approx \lambda_{\text{o}}$ and $\lambda_{\text{q,inn}} \ll \lambda_{\text{i}}$, can be understood from the total energy flux profiles at the divertor entrances. Figure 6 shows the total energy flux density at each divertor entrance for the case No. 4 with $\delta R_{\text{sep}} = 2$ mm.

The parallel area at each midplane was chosen to divide the heat flux at the divertor entrances Q_{dive} on each side. Positive values of the fluxes are in the direction shown by the arrows in figure 6(*c*).

As shown in figure 6(*a*), the total energy flux density at the UOD entrance is well-reproduced by the exponential function
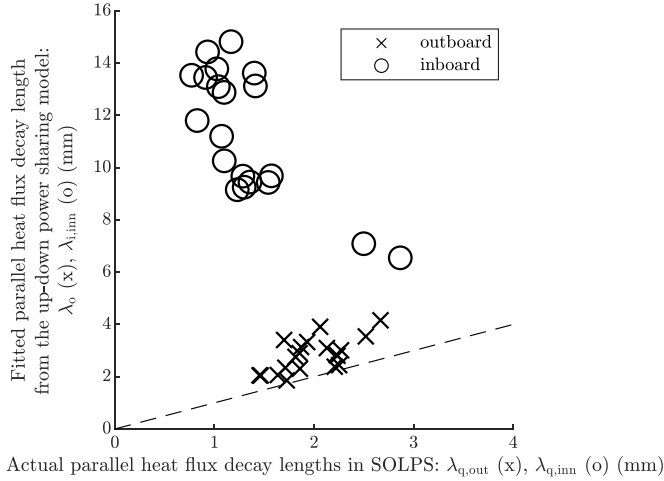
Figure 5. Relationships between the actual parallel heat flux decay lengths $\lambda_{q,out/inn}$ calculated from the total energy flux density profiles in SOLPS-ITER and the fitted parallel heat flux decay lengths $\lambda_{o/i}$ obtained by fitting the up-down power-sharing to Brunner's model, equations (6) and (7). The dashed line shows $\lambda_{q,out} = \lambda_o$ (or $\lambda_{q,inn} = \lambda_i$), which indicates the up-down sharing can be estimated from the parallel heat flux decay length or vice versa.

and that at the lower-outer divertor entrance is almost on top of it. This picture matches with the assumption of Brunner's model about the energy fluxes towards the upper and the lower divertors, thus we have obtained $\lambda_{q,out} \approx \lambda_o$ for the outboard side.

This picture does not hold on the inboard side though, as shown in figure 6(*b*). Unlike figure 6(*a*), the energy flux densities at the upper- and the lower-inner divertor entrances do not share a similar profile in the secondary SOL.

There are two reasons for the mismatch between the total energy flux density profiles at A and C in figure 6(*c*) in the secondary SOL. One is the contribution of the convective part of the energy flux. In the inner secondary SOL, there is a convective energy flow upwards, which forms the bump of the total energy flux density at the UID entrance in the secondary SOL and reduces the total energy flux at the lower-inner divertor entrance. The other reason is the additional power source from the outboard side through the primary SOL, crossing the surface 'e' in figure 6(*c*). Looking at the values at the primary separatrix, the value at the UID entrance ($\sim$1100 MW m^{-2}) is much higher than that at 'e' ($\sim$200 MW m^{-2}). This indicates that the energy flux at the UID entrance in the primary SOL is dominantly due to the power through the inboard side of the primary separatrix. On the other hand, the energy flux density at the lower-inner divertor entrance in the secondary SOL appears to gain by the power source from the outboard side through the primary SOL, as shown by the dashed black arrow in figure 6(*c*). For the above two reasons, we have obtained $\lambda_{q,inn} \ll \lambda_i$—the fraction to the upper divertor is much smaller (i.e. λ_i is much larger) than that expected from Brunner's model using the parallel heat flux decay length at the UID entrance $\lambda_{q,inn}$. It should be noted that the negative value of the energy flux density at 'e' is due to the convective flow, which will be addressed in section 4.2.3.2.

4.2. IN-OUT power-sharing

As already shown in figure 3(*a*), the power fraction to the inner divertors did not increase with δR_{sep} in the SOLPS result, whereas it showed a clear increase with increasing δR_{sep} in the experiments [4, 9].

Why would the power fraction to the inboard side, 'f_i', change with δR_{sep}? The change must be explained by (1) the ratio of radial heat transport through the primary separatrix between the HFS and the LFS and/or by (2) a difference in the main SOL losses with δR_{sep} and/or by (3) the in-out power-sharing in the primary SOL (between the two separatrices). Each of those points is discussed in this section.

4.2.1. Radial heat flux through the primary separatrix.
To understand whether any mechanism dominates, we first assess (1) the ratio of radial energy transport through the primary separatrix between HFS and LFS. Figure 7 shows the ratio $P_{sep,HFS}/P_{sep}$ obtained in the simulations for $0 \leqslant \delta R_{sep} \leqslant 4$ mm. It is clearly seen that the ratio is lower in the DDN cases (0 mm $< \delta R_{sep}$) compared to the CDN cases ($\delta R_{sep} = 0$ mm).

To understand why it is lower in DDN than in CDN, we first decompose the radial transport into conduction and convection, plotting them along the primary separatrix in the clockwise direction from the bottom, as shown by the coordinate $s_{pol,sep}$ in figure 8(*a*). Figure 8(*b*) shows the profiles of the radial heat flux density $q_\perp$ for $\delta R_{sep} = 0$ mm and $\delta R_{sep} = 1$ mm of Case No. 4, as representatives of CDN and DDN, respectively. A pronounced difference of the total heat flux density between CDN and DDN is seen in the bottom half of the HFS 0 m $\leqslant s_{pol,sep} \leqslant 5$ m, the region circled by the dashed lines and named 'X' in figure 8(*a*). By decomposing it into conduction (solid lines) and convection (dotted lines), we find that the difference is dominantly due the conduction, which leads us to focus on the radial conductive heat flux density.

The radial conductive transport is dominated by the anomalous transport. Since we set poloidally constant anomalous radial heat conduction coefficients, $\chi_\perp = \chi_{e\perp} = \chi_{i\perp}$, the radial conductive heat flux density $q_{\perp,cond}$ is given by

$$q_{\perp,cond} = -n\chi_\perp \frac{d(T_e + T_i)}{dy} = -n\chi_\perp \frac{dT}{dy}, \qquad (13)$$

where n is the plasma density, T_e and T_i are the electron and ion temperature respectively, and y is the radial coordinate. Figures 8(*c*) and (*d*) respectively show the decomposed parts of $q_{\perp,cond}$, the temperature gradient dT/dy and the plasma density n. In the region X, 0 m $\leqslant s_{pol,sep} \leqslant 5$ m, both of them are larger in CDN than in DDN, contributing to the larger $q_{\perp,cond}$ in the region.

Let us consider the parallel energy flux along the first flux tube surrounding the primary separatrix and resulting temperature profile. There is a fundamental difference between CDN and DDN in terms of the stagnation point of the parallel energy flux which we call 'upstream' here. In CDN, the 'upstream' of the energy flux in the region X is around the inner midplane given the up-down symmetry. In DDN, on the other hand, as shown by the dashed arrow in figure 8(*a*), the 'upstream'
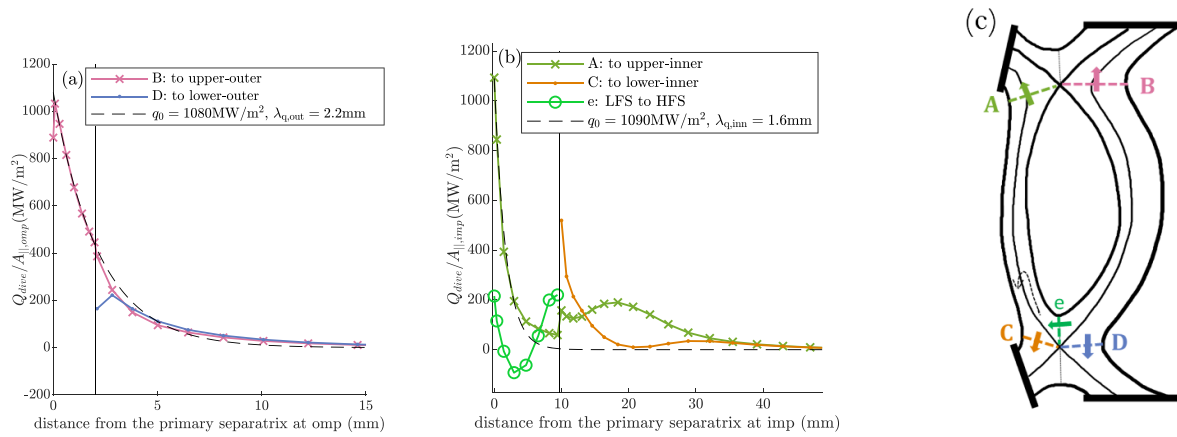
Figure 6. Total energy flux density at the OMP, obtained by dividing the total energy flux at each divertor entrance with the parallel area at each midplane: (*a*) the outer divertor entrances and (*b*) the inner divertor entrances. Results shown are for the case No. 4 with $\delta R_{\text{sep}} = 2$ mm.
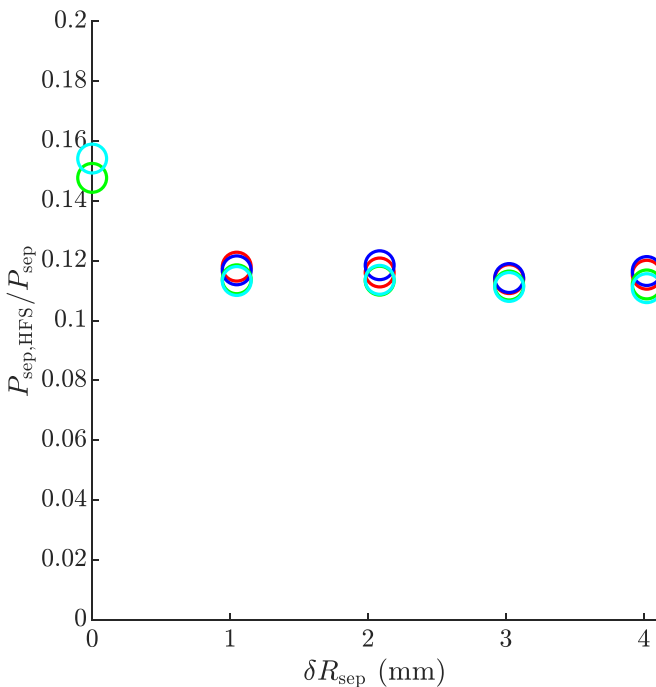
Figure 7. Ratio of the total energy through the primary separatrix on HFS, $P_{\text{sep,HFS}}/P_{\text{sep}}$.

of the energy flux flowing in the region X $q_{\parallel\text{DDN}}$ is located around the OMP on the LFS as in SN, as the most of the power from the separatrix comes out at OMP. This difference leads us to expect $|q_{\parallel\text{DDN}}| > |q_{\parallel\text{CDN}}|$ as the radial power on the LFS is larger than that on the HFS. In addition, due to the different location of the 'upstream', the connection length from the upstream to the corresponding target between DDN and CDN differ. It is approximately a factor five larger in DDN in this case. Given the two-point model, $T_{\text{u}}^{7/2} \propto L_{\parallel}q_{\parallel}$, those two differences make the upstream temperature in CDN lower than that in DDN. Assuming that (1) the temperature in the region X is similar to the temperature at the OMP in DDN and

(2) the temperature along the last closed flux surface (LCFS) is identical between CDN and DDN, this difference in the upstream temperature makes the radial temperature gradient in the region X higher in CDN compared to DDN. In addition, in the region X of CDN, there is a clear temperature drop towards the bottom X point, which is likely to be caused by an extra radial power loss to the PFR region in the flux tube below the X-point. This makes the significant difference in dT/dy between CDN and DDN in the region X. It appears that the density profiles have peaks near the X-points in figure 8(*d*) in order to reduce the pressure gradient generated by the temperature drops.

Through these ways, the in-out power-sharing between CDN and DDN can vary because of the radial transport through the primary SOL. In the investigated cases in this paper, the power fraction to the inboard side f_{i} was reduced from CDN to DDN mainly because of the reduced radial temperature gradient on the bottom half region of the HFS.

4.2.2. Power loss in the main SOL. In this section we consider (2) a difference in the main SOL losses with δR_{sep}, by confirming the energy balance in the region from the primary separatrix to the 4 divertor entrances. We consider two power loss mechanisms in the region, the volumetric radiation power loss P_{rad} and the power flowing through the plasma to the side wall (leaving the plasma grid) P_{sdw}. As shown in figure 9, the power balance in the region is satisfied with less than 10% contribution of P_{rad} and almost no contribution of P_{sdw}.

Given that neither (1) the radial heat transport nor (2) the main SOL losses explains the behaviour of f_{i} in the DDN cases, we look into the parallel heat transport in the primary SOL in the next section.

4.2.3. The role of parallel heat flux through the primary SOL. To discuss in-out power-sharing in the primary SOL, we define the power crossing the upper divertor entrances through the primary SOL as $P_{\text{pri,i}}$ and $P_{\text{pri,o}}$ for the inner and outer,
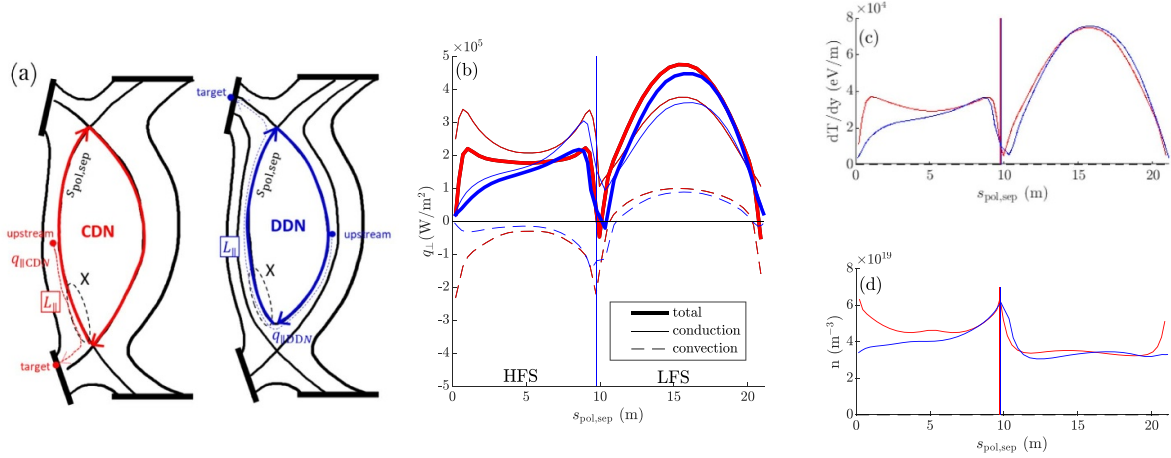
Figure 8. Profiles related to the radial heat flux densities for Case No. 4 along the primary separatrix. The red lines ($\delta R_{\text{sep}} = 0$ mm) represent the CDN cases while the blue lines ($\delta R_{\text{sep}} = 1$ mm) represent the DDN cases. (*a*) The coordinate $s_{\text{pol,sep}}$ along the primary SOL, (*b*) the radial heat flux densities: total (thick solid), conduction (solid), convection (dashed), (*c*) the radial temperature gradient ($T = T_{\text{e}} + T_{\text{i}}$), (*d*) the plasma density.
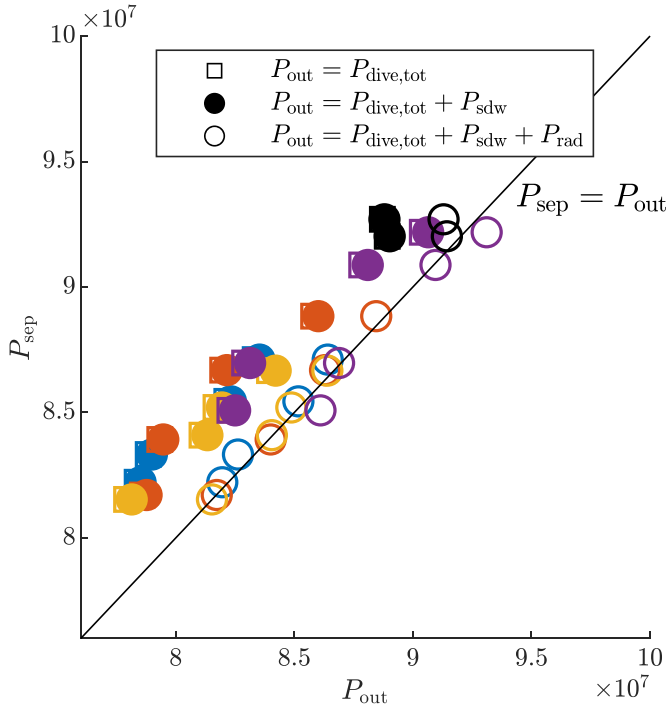
Figure 9. Power coming into the SOL region (= Power crossing the primary separatrix P_{sep}) v.s. power getting out from the SOL region P_{out}. Markers show P_{out} accounting progressively for 3 contributions: the power crossing through the divertor entrances $P_{\text{dive,tot}}$, the power following to the side walls P_{sdw}, and the volumetric power loss by radiation P_{rad}. The colors are for δR_{sep}; black: 0 mm, blue: 1 mm, orange: 2 mm, yellow: 3 mm, purple: 4 mm.

respectively, and the in-out power ratio as $K_{\text{i,pri}} \equiv P_{\text{pri,i}}/P_{\text{pri,o}}$ (see figure 10(*a*)). Figure 10(*b*) shows a summary of this section—the in-out power ratio $K_{\text{i,pri}}$ obtained by SOLPS (colored markers) appears to be lowered by two effects, (1)

the total flux compression from the OMP to the UID and (2) the parallel current inducing anti-clockwise heat transport in the primary SOL. Those two effects are discussed in detail in the following subsections.

4.2.3.1. The effect of total flux expansion/compression. In this section we assess the effect of total flux expansion/ compression of $|\mathbf{B}|$ along a flux tube on $K_{\text{i,pri}}$. As shown in figure 10(*a*), we assume all of the power through the primary separatrix comes out at the OMP and it is separated into $q_{\|\text{OMP}_{\text{o}}}$, the parallel energy flux density flowing to the outer divertor, and $q_{\|\text{OMP}_{\text{i}}}$, that to the inner divertor, on each flux tube. If there is no volumetric power gain/loss and no radial transport in the flux tube, the ratio of the power through the primary inner divertor entrance to that through the primary outer divertor entrance, defined as $k_{\text{i,pri}}$, should be equal to $q_{\|\text{OMP}_{\text{i}}}/q_{\|\text{OMP}_{\text{o}}}$, such that

$$k_{\text{i,pri}} = \frac{q_{\|\text{OMP}_{\text{i}}}}{q_{\|\text{OMP}_{\text{o}}}}. \tag{14}$$

The difference between the newly-defined lower-case $k_{\text{i,pri}}$ and the upper-case $K_{\text{i,pri}}$ is that the former is the ratio for a single flux tube in the primary SOL, while the latter is for the integrated value of all the flux tubes in the primary SOL, as will be precisely described in equation (18). With the additional assumptions that (1) conduction dominates the parallel heat transport, (2) target temperatures are low enough to satisfy $T_t^{7/2} \ll T_u^{7/2}$, and (3) the strength of the total magnetic field $|\mathbf{B}| = B$ is constant along the flux tube, Pitcher & Stangeby's model [14] would lead us to expect

$$\frac{q_{\|\text{OMP}_{\text{i}}}}{q_{\|\text{OMP}_{\text{o}}}} \sim \frac{L_{\text{o}}}{L_{\text{i}}} \equiv k_1, \tag{15}$$

where L_{o} and L_{i} are the parallel distances from the OMP to the outer and inner divertor targets, respectively (see figure 10(*a*)).
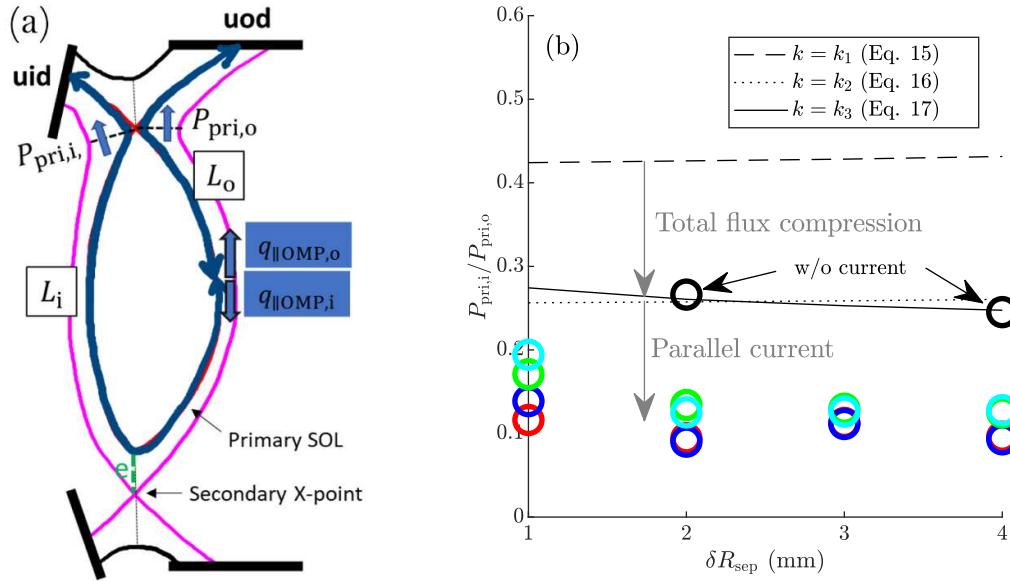
Figure 10. (*a*) Schematic view of the primary SOL and definition of the in-out power-sharing in the primary SOL. (*b*) In-out power-sharing in the primary SOL in SOLPS-ITER simulations (colors as in table 2). The estimations obtained by equation (18) for *k* given by one of equations (15)–(17); dashed: $k = k_1$ (equation (15)) i.e. estimation by the connection length ratio, dotted: $k = k_2$ (equation (17)) i.e. estimation accounting for B-variation with liner approximation, solid: $k = k_3$ (equation (16)) i.e. estimation accounting for B-variation with full integration.

The third assumption above, however, is not well satisfied in STs. Accounting for the *B*-variation, i.e. flux expansion/compression, changes the ratio as [15]

$$\frac{q_{\parallel\mathrm{OMP_i}}}{q_{\parallel\mathrm{OMP_o}}} \sim \frac{\int_{\mathrm{OMP}}^{\mathrm{uod}} \frac{B}{B_{\mathrm{OMP}}}\mathrm{d}s}{\int_{\mathrm{uid}}^{\mathrm{OMP}} \frac{B}{B_{\mathrm{OMP}}}\mathrm{d}s} \equiv k_3. \tag{16}$$

By assuming (1) |**B**| is inversely proportional to the radial coordinate *R* and (2) *R* is linear with the parallel distance, the ratio can be described with the toroidal flux expansion/compression, $f_{R_o} \equiv B_{\mathrm{OMP}}/B_{\mathrm{ot}} \sim R_{\mathrm{ot}}/R_{\mathrm{OMP}}$ and $f_{R_i} \equiv R_{\mathrm{it}}/R_{\mathrm{OMP}}$, where R_{OMP}, R_{ot}, and R_{it} are respectively the radii at the outer midplane, the upper-outer target, and the upper-inner target of the flux tube, such that

$$\frac{q_{\parallel\mathrm{OMP_i}}}{q_{\parallel\mathrm{OMP_o}}} \sim \frac{L_o}{L_i}\frac{f_{R_i}-1}{\ln(f_{R_i})}\frac{\ln(f_{R_o})}{f_{R_o}-1} \equiv k_2. \tag{17}$$

Since this power ratio (equations (15)–(17)) varies between the individual SOL flux tubes in the primary SOL, a way to average them is required to evaluate the net $K_{\mathrm{i,pri}}$. For this, we weight our estimate for the integrated $K_{\mathrm{i,pri,est}}$ towards those flux tubes which carry more power. We assume the power to be divided at the OMP has an exponential-decay form $P\exp(-r_{\mathrm{sep}}/\lambda_q)$, where r_{sep} is the radial distance from the primary separatrix. Using this assumption, the averaged estimation with equation (15) (for example) is

$$K_{\mathrm{i,pri,est}} \equiv \frac{\int_0^{\delta R_{\mathrm{sep}}} P\exp(-r_{\mathrm{sep}}/\lambda_q)\frac{k}{1+k}\mathrm{d}r_{\mathrm{sep}}}{\int_0^{\delta R_{\mathrm{sep}}} P\exp(-r_{\mathrm{sep}}/\lambda_q)\frac{1}{1+k}\mathrm{d}r_{\mathrm{sep}}}, \quad k = k_1, k_2, k_3. \tag{18}$$

In figure 10(*b*), the lines are the averaged estimations from equation (18) with *f* given by one of equations (15)–(17). The estimation by the connection length ratio, L_o/L_i, is ∼0.43, whereas that with |**B**|-variation is 0.25∼0.28, which means the power fraction to the inner divertor was reduced by the flux expansion/compression. This is a benefit for STs that tend to have strong total flux compression $B/B_{\mathrm{OMP}} > 1$ on the HFS. The approximate form of the magnetic field strength with the factor g_{fR} (equation (17)) gives us a similar value to the full estimation with the original formula (equation (16)), with a relative error <10%.

4.2.3.2. Contribution of the parallel current. As shown in figure 10(*b*), simulations performed without the parallel current showed an increase of the in-out power ratio in the primary SOL, $K_{\mathrm{i,pri}}$, which implies the parallel current reduced $K_{\mathrm{i,pri}}$ in the originally investigated cases (colored markers in figure 10(*b*)). Contribution of the parallel current to the total heat flux has been shown both in an experimental study [16] and in a simulation study [17]. To understand the mechanism of the parallel current in this study, we first decompose the total heat flux into the total conduction Q_{cond}, the total convection Q_{conv}, and the energy flux carried by the electron thermal current Q_{thermj}, following equation (9). Figure 11 shows the decomposed parallel heat flux crossing the upper divertor entrances through the primary SOL. As figure 11(*a*) shows, the total heat flux crossing the inner divertor entrance through the primary SOL is reduced by the convective heat flux that flows in the opposite direction. This convective heat flux increases the total heat flux at the outer divertor entrance (figure 11(*b*)), though it is a much smaller fraction of the total heat flux compared to that at the inner divertor entrance.
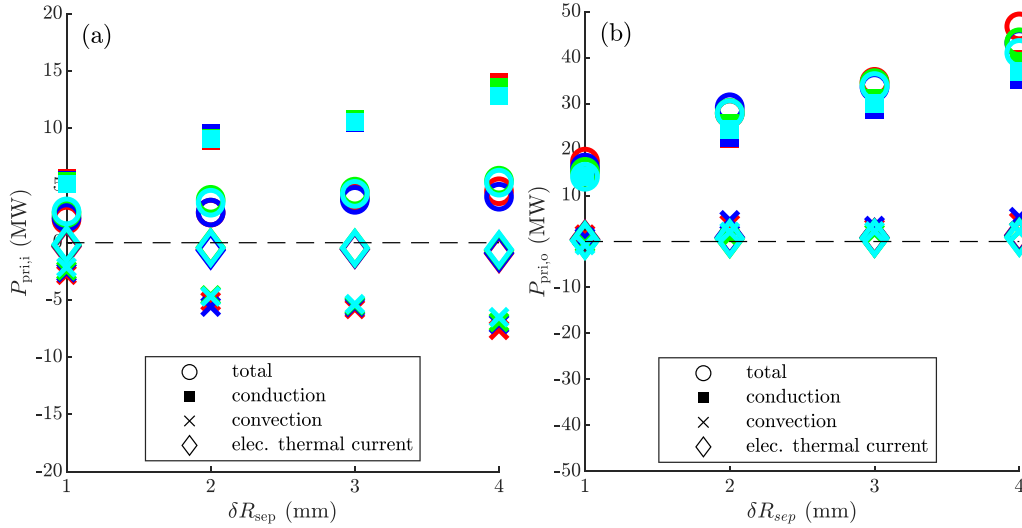
Figure 11. Decomposition of the total heat flux at the divertor entrances of the primary SOL. Positive values: the direction is towards the respective target.

To understand why the convective flux is flowing in the direction that reduces the power to the inner divertor—from the HFS to the LFS—we decomposed the total convective flux into that of electrons and that of ions as introduced in equation (11).

The terms of equation (11) at the UID entrance and at the secondary X-point are shown in figure 12 as a function of $\delta R_{\rm sep}$. At both locations, the strongest contribution to the convective flow is from the parallel current $j_\parallel$ which flows from LFS to HFS. The strong contribution at the location 'e' (marked in figure 10(*a*)) directly tells us that the parallel current in the primary SOL surely reduced $K_{\rm i,pri}$ in the investigated cases. It should be noted that the electron thermal current $Q_{\rm thermj}$ in equation (12) has the same contribution as the current-induced convective term in equation (11), but the effect is a factor ∼3.5 smaller due to the prefactor 0.71 instead of the one for the convective term $5/2$.

Figure 13(*a*) shows the parallel current density in the primary SOL at the surface 'e' for all the cases. We can confirm that the parallel current flows from the LFS to the HFS in all the cases. There is no clear dependence on $\delta R_{\rm sep}$.

In order to understand the physical mechanism of these currents, we integrate Ohm's law for the parallel current density $j_\parallel$ [A m^{-2}] along a flux tube from the UOD target to the UID target (UOD), which gives us

$$j_\parallel = \frac{\bar{\sigma}_\parallel J}{L_\parallel}, \quad J \equiv \left[-(\phi_{\rm uid} - \phi_{\rm uod}) + 0.71(T_{\rm e,uid} - T_{\rm e,uod}) \right.$$
$$\left. + \int_{\rm uod}^{\rm uid} \frac{1}{n} \frac{{\rm d}p_{\rm e}}{{\rm d}s} {\rm d}s \right], \quad (19)$$

where $\bar{\sigma}_\parallel$ [$\Omega^{-1}\,{\rm m}^{-1}$] is the parallel electron conductivity, $L_\parallel$ [m] is the connection length from the UOD to the UID, ϕ [eV] is the potential, $T_{\rm e}$ [eV] is the electron temperature, n is the plasma density, $p_{\rm e}$ [eV m^{-3}] is the electron static

pressure, and s is the parallel coordinate along the flux tube. J determines the direction of the current—a positive value of J (equally, $j_\parallel$) means that the current flows from the LFS to the HFS. In J, the first term represents the thermal current flowing from a hot target to a cold target. The second term is the thermal force on the ions, which pushes ions in the direction of positive electron temperature gradient. The third term represents the pressure gradient force pushing electrons faster than the ions, which produces the net current in the opposite direction of the electron flow.

Figure 13(*b*) shows the individual terms of J in equation (19) for Case No. 1 as a function of $\delta R_{\rm sep}$. For simplicity, only those along the 3rd flux tube outward from the primary separatrix in the numerical grid are shown as representative. It is clearly seen that the 3rd term of J, the term with the electron static pressure gradient, is dominant over the other terms. This suggests that the electron pressure gradient and the plasma density play the key roles on the parallel current along the flux tube.

Figure 14 shows the profiles of the plasma density $n_{\rm e}$ and the electron static pressure $p_{\rm e}$ along the 3rd flux tube from the UID to the UOD. If both profiles were symmetric between the two targets, the term $\int_{\rm uod}^{\rm uid} \frac{1}{n} \frac{{\rm d}p_{\rm e}}{{\rm d}s} {\rm d}s$ would be zero. In other words the positive value of the term is induced by the asymmetry of those profiles. Since we integrate from the UOD to the UOD, the pressure drop towards the UOD makes the term larger with positive values of $\frac{{\rm d}p_{\rm e}}{{\rm d}s}$, while that towards the UOD makes it smaller. The density profile adds a weight to the pressure gradient at each location. In this case, the lower density near the UOD weights more the positive values of $\frac{{\rm d}p_{\rm e}}{{\rm d}s}$ there, while the higher density near the UID weights less the negative values of $\frac{{\rm d}p_{\rm e}}{{\rm d}s}$ on the other side. This is how the term $\int_{\rm uod}^{\rm uid} \frac{1}{n} \frac{{\rm d}p_{\rm e}}{{\rm d}s} {\rm d}s$ has got a positive value. In addition to the asymmetry between the two divertor regions, a clear increase of the electron static pressure from the IMP to the upper-inner divertor entrance (UIDE) in figure 14 contributed to the relatively
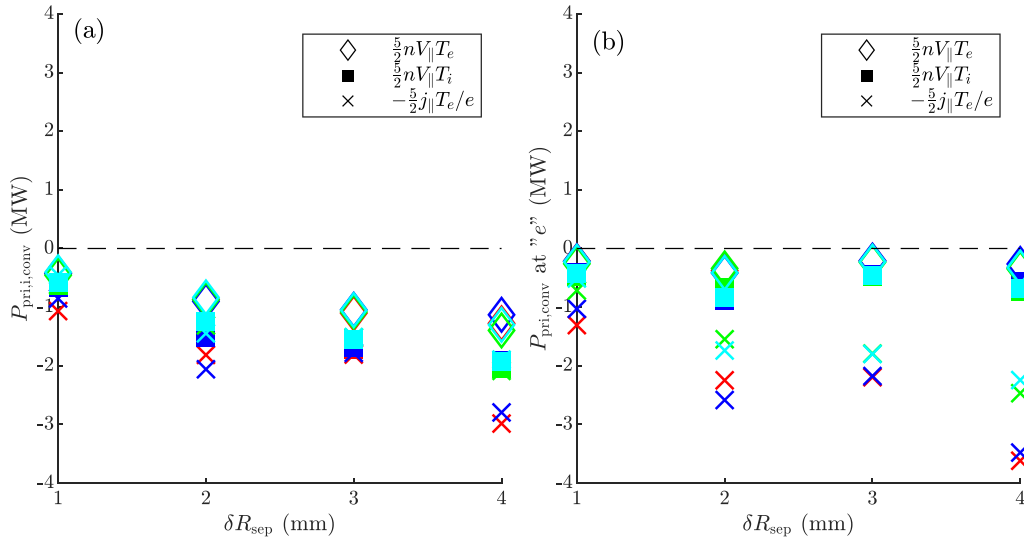
Figure 12. Decomposition of the parallel convective heat flux in the primary SOL (*a*) at the upper-inner divertor entrance and (*b*) at the surface at the secondary X-point, 'e' (as shown in figure 10(*a*)).
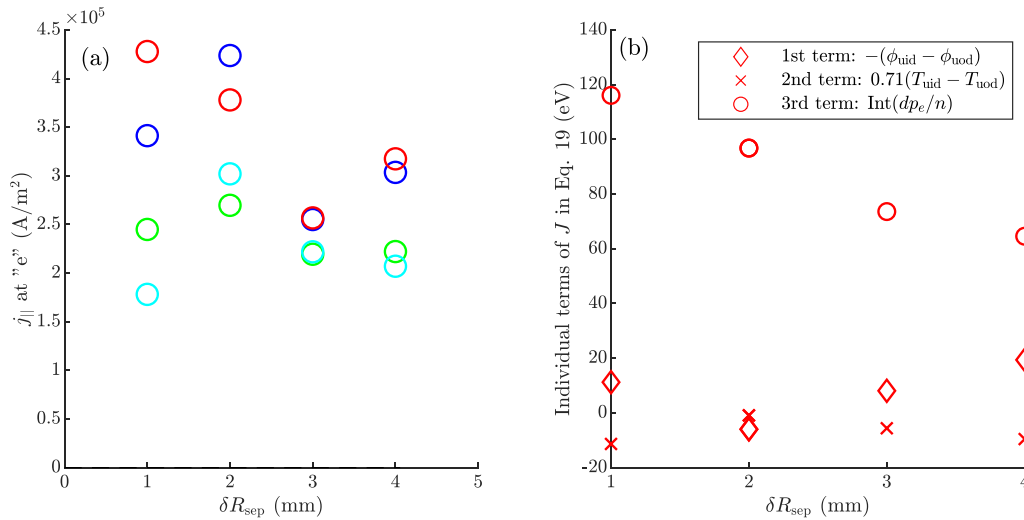

Figure 13. (*a*) Parallel current density at the surface 'e' (shown in figure 10(*a*)) in the primary SOL. (*b*) Individual terms of J in equation (19) for the 3rd flux tube in the primary SOL for Case No. 1.

large value of the term $\int_{\text{uod}}^{\text{uid}} \frac{1}{n} \frac{dp_e}{ds} ds$ because the weight from the plasma density is high (i.e. the density is low) in the region. In section 5 it will be discussed how the pressure gradient became positive from the IMP to the UIDE.

As already shown in figure 10(*b*), the effect of the parallel current has been confirmed by two simulations with the parallel current artificially zeroed out. As shown by the black points, in the absence of the parallel current, we obtained ∼110% increase of the in-out power ratio $P_{\text{pri,i}}/P_{\text{pri,o}}$ in the primary SOL, which results in ∼40% increase of the power fraction to the inner divertors (not shown in this paper).

However, one important question is how universal this contribution of the parallel current would be in the future operational scenarios. Assuming that there should be some pressure

gradient near the both targets in the operational scenarios, a key to obtain this parallel current from the UOD to the UID is a high density near the UID. This is likely to be the case for a case with high-recycling primary inner divertor, but not for a fully-detached case. It is implied also from figure 13(*a*) that the parallel current in the primary SOL is smaller in more detached cases—in figure 13(*a*) the cyan markers are the most detached cases whereas the red markers are the least detached cases as shown in table 2. From those results, the parallel current may not be expected in fully-detached scenarios or in attached (i.e. low-recycling) scenarios, but it might appear in a high-recycling regime for the primary inner divertor, leading it to a deeper detachment by transporting convective heat flux from the inner divertor to the outer divertor.
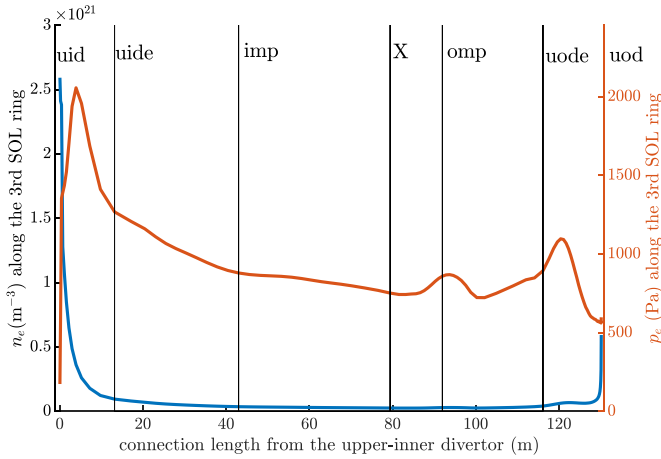
Figure 14. Spatial profiles of the plasma density n_e and the electron static pressure p_e along the 3rd flux tube in the primary SOL from the upper inner divertor (UID) to the upper outer divertor (UOD).

5. Discussion

5.1. The electron static pressure along a flux tube in the primary SOL on the HFS

Why is the electron pressure gradient positive from the inner midplane (IMP) and the UIDE as shown in figure 14? This appears to be a result of the net parallel momentum gain in the flux tube due to the radial transport of the parallel momentum, which is caused by the flow reversal in the primary SOL. The blue solid line in figure 15(*a*) shows the total pressure (dynamic pressure of ions + viscosity + ion/electron static pressure) profile along the 3rd flux tube in the primary SOL from as defined as the coordinate *s* in figure 15(*b*). The total pressure increases from the IMP to $s \sim 45$ m, which appears to be gained by the parallel momentum source due to the net radial flux of convection and viscosity $S_{m\parallel RT}$, shown by the blue dashed line. The net radial momentum flux depends on the radial gradient of the parallel velocity, thus the second radial derivative of the parallel velocity, plotted with the orange line, shows a good correlation with $S_{m\parallel RT}$. The interpretation of this momentum source is given in figure 15(*b*). In the investigated cases, due to the strong recycling source at the upper inner divertor, the plasma flow is reversed in the primary SOL in the region from the UID to the IMP. With $V_\parallel < 0$, a positive value of $d^2 V_\parallel / (dr^2)$ at the 3rd flux tube means that the negative momentum source from the 2nd flux tube is smaller than the negative momentum loss to the 4th flux tube, under the assumption that the radial transport is constant and pointing outwards. As shown in figure 15(*b*), this brings a net radial loss of negative parallel momentum, i.e. a gain of positive parallel momentum. Although it is not necessarily the electron static pressure that is gained by the momentum source, this mechanism in the flow reversal condition appears to be a possible explanation for the positive electron pressure gradient towards the upper inner divertor and resulting parallel current flowing from the LFS to the HFS in the primary SOL.

5.2. Effect of the ballooning effect on the power-sharing

In this study, we chose spatially constant coefficients for the radial transports as mentioned in section 2. In reality, however, the coefficients are likely smaller on the HFS given that there is much less turbulent activity seen on the HFS than on the LFS, as reported in [18]. The fact that we obtained higher fraction to the inner divertors compared to the experimental results especially at CDN could be due to this choice of constant radial transport coefficients.

To investigate how the power-sharing can be affected by spatially-varying radial transport coefficients, we activated the ballooning effect in the SOLPS-ITER code, i.e. used all the radial coefficients ($D_\perp$ and $\chi_\perp$ for the ions and electrons) varying inversely to the *k*th power of the magnetic field $\propto 1/B^k$, on Case No. 2 in table 2. Figures 16(*a*) and (*b*) show the profiles of the radial heat transport coefficient $\chi_\perp$ for the original case and the new case with $k = 1$ along the IMP and the OMP, respectively, and (*c*) shows the power fraction to the inner divertors f_i of those cases. The activation of the ballooning effect reduced f_i around 40% compared to the original cases. This brought f_i down to $\sim$10% for the $\delta R_{sep} = 1$ mm case, which is more consistent with the experimental results compared to the original result without the ballooning effect [6, 9].

As for the up-down sharing, the same ballooning effect decreased the power fraction to the primary divertor up to $\sim$5% on the outboard side (i.e. increased λ_o), whilst increasing it up to $\sim$5% on the inboard side (i.e. decreased $\lambda_{i,inn}$), as shown in figure 17. These tendencies are consistent with the fact that the heat decay length with the ballooning effect is expected to be larger than the original case on the HFS due to the larger radial heat transport coefficient and vise versa on the LFS.

To summarise, the ballooning effect has an impact both on the in-out and the up-down power-sharing, and the values obtained by the simulations got closer to those on the experiments by applying it with the factor $k = 1$. Therefore the activation of the ballooning effect in SOLPS-ITER simulations is recommended for further comparison of the power-sharing with experimental results, but further work is required to specify a proper factor.

5.3. Effect of drifts on the power-sharing

Effects due to the drifts have been recently assessed by SOLPS-ITER simulations on (1) MAST and on (2) STEP.

On the (1) MAST simulations, δR_{sep} was scanned from $\sim$$-2\lambda_q$ to $\sim$$+2\lambda_q$, where λ_q here is the parallel heat flux decay length, and the scan was performed with and without drifts. While the drifts did not noticeably affect the up-down sharing, they affected the in-out power-sharing in a way that ExB drift in the PFR appears to dominate over the ExB drift in the SOL. Further analysis including comparison to experiments is ongoing and will be presented elsewhere. To extend these results to STEP, it should be noted that MAST has a factor
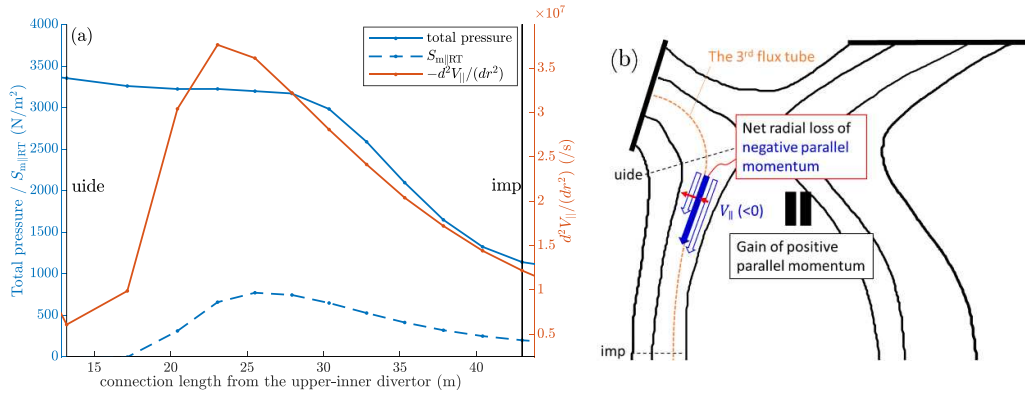
Figure 15. (*a*) Spatial profiles of the total pressure (dynamic pressure of ions + viscosity + ion/electron static pressure), the parallel momentum source due to the net radial flux of convection and viscosity $S_{m\parallel RT}$, and the second derivative of the parallel velocity $d^2V_\parallel/dr^2$ along the third flux tube in the primary SOL from the UIDE to the IMP. (*b*) Schematic view of the relationship between the momentum source $S_{m\parallel RT}$ and $d^2V_\parallel/dr^2$.
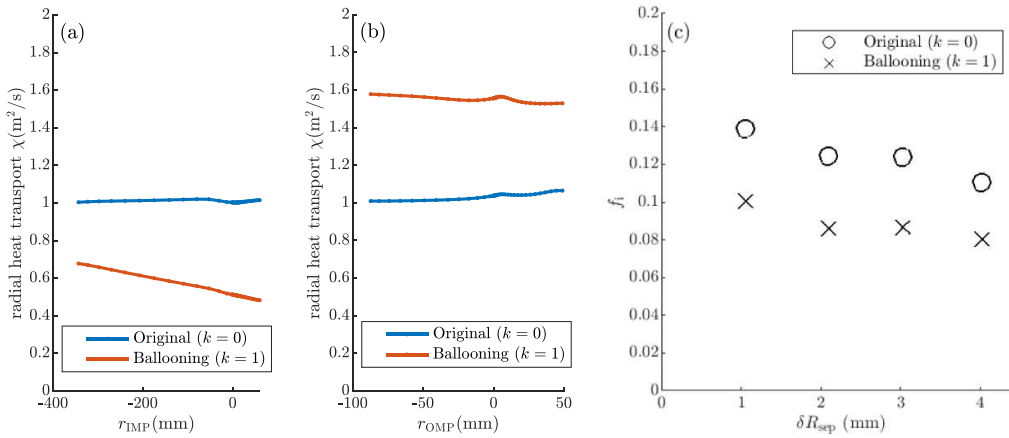
Figure 16. The profiles of the radial heat transport coefficient χ for the original case without the ballooning effect ($k=0$) and the new case with the ballooning effect ($k=1$) at (*a*) the IMP and (*b*) the OMP. (*c*) the power fraction to the inner divertors f_i of Case No. 2 for DDN in table 2 with/without the ballooning effect activated.
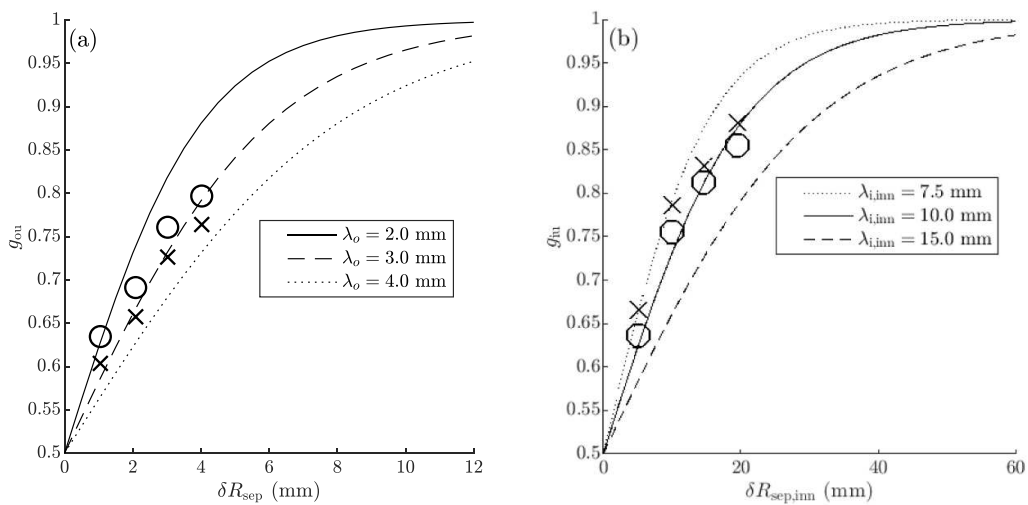
Figure 17. Power fraction to the upper divertor for (*a*) the outboard side, g_{ou} and (*b*) the inboard side, g_{iu}. Circles: original ($k=0$), crossings: ballooning ($k=1$).

7–8 weaker magnetic field and about a factor 10 lower density compared to STEP.

The (2) STEP simulations were performed on the same CDN configuration as this paper, but in pure D with a simplified representation of impurity radiation. In terms of the up-down power-sharing, there is a noticeable increase of the power fraction to the upper divertor on the HFS by the activation of the drifts, which is in line with the expectations based on MAST results [4, 6], while the effect appears to be slight on the LFS. These observations and the physical phenomena behind them will be presented elsewhere, while further simulations with evolving Ar both on CDN and DDN will be assessed in the future.

6. Conclusion

The impact of disconnection of the two separatrices on the power-sharing between the four divertors in a disconnected-double-null configuration was investigated on the initial iteration of the STEP design. Overall, SOLPS-ITER simulation results (without drifts) showed less significant impact on the power fraction to the inner divertors as a function of $\delta R_{sep}/\lambda_q$ compared to the experimental results for current machines. At the highest δR_{sep} the total power fraction to the inner divertors was $\sim$20%, which is similar to the experimental result for MAST [4] and is lower than those on conventional tokamaks. This indicates the benefit of a DN configuration may be less on STEP than what we expected from the previous experiments on conventional tokamaks, in terms of the power loading onto inner divertor targets.

To understand the overall power-sharing, the up-down sharing and in-out sharing were separately investigated. Findings from the up-down sharing are:

- up-down sharing (outer): The dependence of the sharing on disconnection of the two separatrices is well described by Brunner's model. This is because the profiles of the parallel heat flux density at the divertor entrances agree well with what Brunner's model expects. Thus the parallel heat flux decay length obtained in the SOLPS-ITER agrees well with the fitted parallel heat flux decay length from the up-down power-sharing model, which indicates that the actual parallel heat flux decay length on the outboard side is a good indicator of the up-down power-sharing, or vice versa.
- up-down sharing (inner): The dependence of the sharing on disconnection of the two separatrices is well described by Brunner's model, as long as we choose a proper fitting parameter. The fitting parameter is not simply related to the parallel heat flux decay length in the simulation, unlike the outboard side, as the profiles of the parallel heat flux density at the upper- and lower divertor entrances do not match each other in the secondary SOL. This is because of the combined effects—the power radially crossing the HFS primary separatrix and the power coming from the LFS by the parallel transport in the primary SOL. For this reason we obtained much smaller actual parallel heat flux decay length

in the simulation than the fitted parallel heat flux decay length from the up-down power-sharing model. Further study is required to understand the relationship between them.
- Ballooning effect: The ballooning effect with the factor $k = 1$ ($\chi \propto 1/B^k$) decreased the power fraction to the primary divertor (i.e. increased λ_o) up to $\sim$5% on the outboard side, whilst increasing it (i.e. decreased $\lambda_{i,inn}$) up to $\sim$5% on the inboard side.

The in-out power-sharing was discussed separately by (1) the ratio of radial heat transport through the primary separatrix between the HFS and the LFS, (2) power loss in the main SOL, and (3) the in-out power-sharing in the primary SOL (between the two separatrices)

- in-out sharing (1) the radial flux through the primary separatrix: The power fraction to the inboard side was $\sim$12% in DDN and $\sim$16% in CDN. This difference is due to the reduced amount of the conductive (anomalous) part of the radial heat flux along the primary separatrix in the bottom half region on the HFS in DDN, which was mainly due to the smaller radial temperature gradient in that region in DDN compared to CDN. This was caused by two features of the temperature profiles in the first flux tube outward from the primary separatrix on the HFS bottom half region: (1) higher temperature in DDN than in CDN due to the contribution from the parallel heat flux from the LFS and (2) temperature drop from the IMP to the bottom X-point. Since it is a fundamental difference between CDN and DDN, we presume this difference of the in-out power ratio would appear in future simulations when the same profiles of the radial transport coefficients were set for CDN and DDN. However it is remained an open question what would happen in experiments.
- in-out sharing (2) The two power loss mechanism considered—the radiation loss and the power through the plasma to the side walls—had less than 10% contribution in total to the entire power balance.
- in-out sharing (3) the parallel flux through the primary SOL: Using Stangeby & Pitcher's model, we have shown that the flux expansion/compression from the OMP to each divertor target in the STEP design would reduce the power fraction to the inner divertor, which is an operationally useful feature of STs. A further decrease of the power fraction to the inner divertor was obtained by the convective heat flow from the LFS to the HFS induced by the parallel current in the primary SOL. The parallel current is caused by the positive pressure gradient towards the upper-inner target which is occurring together with the plasma reversed flow in the UID region.

  Simulations without parallel current showed a good agreement with Stangeby & Pitcher's model with flux expansion/compression effect. This convinced us that there is the effect of flux expansion/compression on the in-out power-sharing in the primary SOL as estimated by the model, and additionally there is a reduction of the ratio to

the inner by the parallel current. While the latter appears to be case-dependent, we presume the former should be universal for STs.

- Ballooning effect: The activation of the ballooning effect reduced the power fraction to the inner divertors f_i around 40% compared to the original cases. This brought f_i down to $\sim$10% for the CDN case, which is consistent with the experimental results. This suggests the importance of the ballooning effect for further comparative work on the power-sharing between simulations and experiments. The factor $k = 1$ ($\chi \propto 1/B^k$) appears to be a reasonable first choice, but further work is required to specify a proper factor.

For better understanding of the power-sharing in DDN, comparative study between Brunner's model, SOLPS-ITER simulation, and experiments is ongoing on MAST, including the drift terms. Use of more advanced versions of SOLPS-ITER code is also important on this subject. Further studies addressing the effects of the assumed radial transport coefficients and drifts are ongoing on STEP.

Acknowledgments

ORCID iDs

S.S. Henderson ⬛ https://orcid.org/0000-0002-8886-1256
B. Lipschultz ⬛ https://orcid.org/0000-0001-5968-3684

References

[1] Wilson H. *et al* 2020 *Commercialising Fusion Energy* (Bristol: IOP Publishing) pp 8-1–8-18
[2] Braams B.J. *et al* 1985 *Plasma Physics and Controlled Nuclear Fusion Reserach 1984* vol 2 (Vienna: IAEA) p 125
[3] Marchand R., Dumberry M., Demers Y., Cote C., Clair G.L., Larsen J.-M., Bonnin X. and Braams B.J. 1995 *Nucl. Fusion* **35** 297–304
[4] Temmerman G.D., Delchambre E., Dowling J., Kirk A., Lisgo S. and Tamain P. 2010 *Plasma Phys. Control. Fusion* **52** 095005
[5] Kirk A., Ahn J.-W. and Counsell G.F. 2003 *J. Nucl. Mater.* **313-316** 1081–4
[6] Temmerman G.D., Kirk A., Nardon E. and Tamain P. 2011 *J. Nucl. Mater.* **415** S383–6
[7] Petrie T.W. *et al* 1999 A comparison of plasma performance between single-null and double-null configurations during Elming H-mode (available at: www.osti.gov/servlets/purl/766942)
[8] Petrie T.W. *et al* 2001 *J. Nucl. Mater.* **290** 935–9
[9] Brunner D., Kuang A.Q., LaBombard B. and Terry J.L. 2018 *Nucl. Fusion* **58** 076010
[10] Dekeyser W., Bonnin X., Lisgo S.W., Pitts R.A., Brunner D., LaBombard B. and Terry J.L. 2016 *Plasma Fusion Res.* **11** 1403103
[11] Wiesen S. *et al* 2015 *J. Nucl. Mater.* **463** 480–4
[12] Bonnin X., Dekeyser W., Pitts R., Coster D., Voskoboynikov S. and Wiesen S. 2016 *Plasma Fusion Res.* **11** 1403102
[13] Pitts R. *et al* 2019 *Nucl. Mater. Energy* **20** 100696
[14] Pitcher C.S. and Stangeby P.C. 1997 *Plasma Phys. Control. Fusion* **39** 779
[15] Petrie T.W. *et al* 2013 *Nucl. Fusion* **53** 113024
[16] LaBombard B. *et al* 1997 *J. Nucl. Mater.* **241–243** 149–66
[17] Moulton D., Corrigan G., Harrison J.R. and Lipschultz B. 2018 *Nucl. Fusion* **58** 096029
[18] LaBombard B. *et al* 2017 *Nucl. Mater. Energy* **12** 139–47